


RESEARCH

Open Access



# Iron loading is a prominent feature of activated microglia in Alzheimer's disease patients

Boyd Kenkhuis<sup>1,2\*</sup>, Antonios Somarakis<sup>2†</sup>, Lorraine de Haan<sup>3</sup>, Oleh Dzyubachyk<sup>2,5</sup>, Marieke E. IJsselsteijn<sup>3</sup>, Noel F. C. C. de Miranda<sup>3</sup>, Boudewijn P. F. Lelieveldt<sup>2</sup>, Jouke Dijkstra<sup>2</sup>, Willeke M. C. van Roon-Mom<sup>1</sup>, Thomas Höllt<sup>2,4</sup> and Louise van der Weerd<sup>1,2</sup>

## Abstract

Brain iron accumulation has been found to accelerate disease progression in amyloid- $\beta$  (A $\beta$ ) positive Alzheimer patients, though the mechanism is still unknown. Microglia have been identified as key players in the disease pathogenesis, and are highly reactive cells responding to aberrations such as increased iron levels. Therefore, using histological methods, multispectral immunofluorescence and an automated in-house developed microglia segmentation and analysis pipeline, we studied the occurrence of iron-accumulating microglia and the effect on its activation state in human Alzheimer brains. We identified a subset of microglia with increased expression of the iron storage protein ferritin light chain (FTL), together with increased Iba1 expression, decreased TMEM119 and P2RY12 expression. This activated microglia subset represented iron-accumulating microglia and appeared morphologically dystrophic. Multispectral immunofluorescence allowed for spatial analysis of FTL<sup>+</sup>Iba1<sup>+</sup>-microglia, which were found to be the predominant A $\beta$ -plaque infiltrating microglia. Finally, an increase of FTL<sup>+</sup>Iba1<sup>+</sup>-microglia was seen in patients with high A $\beta$  load and Tau load. These findings suggest iron to be taken up by microglia and to influence the functional phenotype of these cells, especially in conjunction with A $\beta$ .

**Keywords:** Alzheimer, Microglia, Iron, Ferritin, Human

## Introduction

Alzheimer's disease is the most common cause of dementia, and is defined by the presence of amyloid- $\beta$  (A $\beta$ ) plaques and tau tangles. In addition, the brain's resident innate immune cells, microglia, have been found to be at the centre-stage of the disease, as most identified risk genes are predominantly or even exclusively expressed in microglia [1, 2].

Not only can microglia modulate Alzheimer's disease, but many transcriptomic studies showed microglia to undergo the most pronounced changes in response to pathology. In mice, a subset of responding microglia has been found to lose their homeostatic molecular signature and transition into a so-called 'disease-associated microglia' (DAM) state [3]. In humans, a comparable yet disparate state coined the human Alzheimer microglia (HAM) has been identified [4]. Upregulated genes in these subsets do not only indicate loss of homeostatic function and increased pro-inflammatory activation, but also dysregulated iron-metabolism, manifested via upregulation of the *FTL*-gene and downregulation of *FTH1* and *SLC2A11* [4, 5]. *FTL* encodes the ferritin light chain (FTL) protein, the component of the major iron-storage complex ferritin,

\*Correspondence: b.kenkhuis@lumc.nl

<sup>†</sup>Boyd Kenkhuis and Antonios Somarakis have contributed equally to this work

<sup>1</sup> Department of Human Genetics, Leiden University Medical Center, Albinusdreef 2, 2333 ZA Leiden, The Netherlands

Full list of author information is available at the end of the article



responsible for the long term storage of iron. These transcriptomic findings coincide with previously observed ferritin<sup>+</sup> microglia in Alzheimer's disease [6, 7]. Though increased iron concentration likely plays a role, the exact link between the two has not yet been established.

Iron accumulation, irrespective of microglial activation, on the other hand, has been reported in disease-affected areas in Alzheimer's disease, using both in-vivo and post-mortem human MRI [8]. Several MRI and histology studies found high correlations between iron accumulation and cortical A $\beta$  and tau spreading [9–11]. Clinically, increased iron concentrations were shown to accelerate cognitive decline in A $\beta$ -positive Alzheimer patients, indicative of a disease-modifying role for iron accumulation [12, 13]. Again, how iron accelerates cognitive deterioration is poorly understood.

Therefore, in this study we aimed to research the possible link between iron accumulation and functionally activated microglia, and finally, its relation with A $\beta$ -plaques. We performed a comprehensive investigation of iron-accumulating microglia, and first identified that the iron-storage protein FTL, specifically reflected increased iron accumulation in microglia. Secondly, by using multispectral immunofluorescence and an in-house automated cell-analysis pipeline, we found FTL<sup>+</sup> microglia to show significant activation, shown via both downregulation of homeostatic markers TMEM119 and P2RY12 and dystrophic morphology, and to predominantly infiltrate A $\beta$ -plaques. This provides evidence for iron dysregulation as a prominent feature of activated microglia in Alzheimer's disease in humans.

## Methods

### Tissue acquisition

Brain autopsy tissue of the middle temporal gyrus (MTG) of 12 Alzheimer patients and 9 age-matched controls was collected at the Leiden University Medical Center (LUMC), Netherlands Brain Bank (NBB) and the Normal Aging Brain collection Amsterdam (NABCA). Patients were included based on clinical presentation and diagnosis was confirmed by a neuropathologist. The neuropathologists also evaluates Braak stage, based on Gallyas and Tau immunohistochemistry (IHC), and Thal phase based on Congo Red and Amyloid Beta IHC, in eighteen standard regions, according to the latest international diagnostic criteria [14–16]. Patient demographics are reported in Additional file 1: Table S1. All material has been collected with written consent from the donors and the procedures have been approved by the Medical Ethical committee of the LUMC and the Amsterdam UMC.

### Histology and immunohistochemistry

Formalin fixed paraffin embedded (FFPE) tissue was serially cut into ten 5- $\mu$ m-thick and four 10- $\mu$ m-thick sections. Consecutive 10- $\mu$ m-thick sections were used for histological detection of iron using an enhanced Perl's stain and IHC detection of Ferritin Light Chain (FTL). 5- $\mu$ m-thick sections were used for staining of the microglia multispectral immunofluorescence (mic-mIF) panel (Additional file 1: Table S2) to verify expression of FTL in microglia/macrophages (Iba1), look at the activation state of these cells (P2RY12/TMEM119) and study the interaction with A $\beta$ -plaques. Finally, of three subjects, 20- $\mu$ m-thick sections were obtained for 3D confocal imaging. Step-by-step histological and IHC optimization protocols, together with the imaging parameters, are reported in the Supplementary Methods. A step-by-step mIF protocol and further analysis of the described histological, IHC and mIF staining will be described in the following sections.

### Microglia multispectral immunofluorescence (mic-mIF) panel

One 5- $\mu$ m-thick section of each subject was stained with the mic mIF panel with the following protocol, based on a previously described protocol by IJsselsteijn et al. [17]. Sections were deparaffinized with 3  $\times$  5 min xylene, rinsed twice in 100% alcohol and subsequently washed with 100% ethanol for 5 min. Endogenous peroxidases were blocked for 20 min in 0.3% H<sub>2</sub>O<sub>2</sub>/methanol, after which the slides were rinsed with 70% and 50% alcohol. Heat induced antigen-retrieval was performed by cooking the slides for 10 min in pre-heated citrate (10 mM, pH=6.0) buffer for 10 min. After cooking, excess buffer was removed and slides were cooled for 60 min. Non-specific antibody binding sites were blocked with blocking buffer (0.1% BSA/PBS + 0.05% Tween) for 30 min. Firstly, slides were incubated with anti-TMEM119 (1:250, Sigma Aldrich) diluted in blocking buffer overnight at RT. Slides were washed thrice with PBS and incubated with Poly-HRP secondary antibody for 30 min. Slides were washed again and incubated with the appropriate Opal tertiary antibody (1:100 in amplification diluent, Perkin Elmer) for 60 min, which causes permanent binding of the fluorophore to the antigen site. All subsequent steps are performed in the dark where possible. Finally, the slides are placed back in citrate buffer and cooked in the microwave for 15 min to wash the primary antibody off. The same steps are repeated for anti-P2RY12 (1:2500, Sigma Aldrich). After binding of the two antibodies amplified with Opal, slides are incubated with a primary antibody mix with anti-FTL (1:100, Abcam), anti-A $\beta$  (17–24) (1:250, Biolegend) and anti-Iba1 (1:20, Millipore)

antibodies, diluted in blocking buffer, overnight at room temperature. The next day, after three washes with PBS, slides are incubated with a secondary antibody mix of G-a-rIgG A594, G-a-mIgG2b A647 and G-a-mIgG1 CF680 (1:200, ThermoFisher), diluted in 0.1% BSA/BPS. Finally, the slides are washed and incubated with 0.1  $\mu\text{g}/\text{mL}$  DAPI (Sigma Aldrich) for 5 min, after which they are mounted with 30  $\mu\text{L}$  Prolong diamond (ThermoFisher).

### Post-mortem MRI acquisition and analysis

MRI data and  $T2^*$ -w severity scores were obtained from a previous study by Bulk et al. [10], on the same tissue-blocks. In this study, tissue blocks were put in proton-free fluid (Fomblin LC08, Solvay), and scanned at room temperature on a 7 T horizontal-bore Bruker MRI system equipped with a 23 mm receiver coil and Paravision 5.1 imaging software (Bruker Biospin, Ettlingen, Germany). A gradient echo scan was acquired with repetition time = 75.0 ms, echo time = 33.9 ms, flip angle = 25° at 100  $\mu\text{m}$  isotropic resolution with 20 signal averages. Subsequently, cortices were assessed for changes in MRI contrast following a pre-defined scoring system.

### Iron-positive cell identification

Whole slide scans of the histochemical iron staining were exported from Philips Intellisite digital Pathology Solution platform (Philips, the Netherlands) and imported into ImageJ. RGB images were converted into 8-bit greyscale images. Subsequently, while blinded for diagnosis, for each subject an optimal threshold was set to include DAB-positive intracellular iron depositions, but exclude extracellular background signal. The cortex of the MTG was delineated and the number of positive cells was determined using the ImageJ particle analyser, with a size threshold of 4–100 pixels. Subject AD5 was excluded from this analysis, as iron-accumulating cells could not be distinguished due to high extracellular iron load.

### Single cell segmentation

Identification of the different microglia types was based on the amount of expressed proteins over the segmented area (Additional file 1: Fig. S2a). Hence, accurate segmentation of the whole microglia cell area is of paramount importance for our method. Solutions currently available for microglia cell segmentation (Abdolhoseini et al. 2019 [18], Inform, PerkinElmer) typically fall short of capturing the whole microglia area (Additional file 1: Fig. S2b). These are focused on either capturing the skeleton of the cells, without properly identifying the cell boundaries (Additional file 1: Fig. S2c), or segmenting the microglia's soma excluding their processes, which in the acquired 2D images are typically detached from the soma (Additional file 1:

Fig. S2d). As a result, a novel segmentation algorithm for this type of data was developed.

Identification of the entire cytoplasmic area of microglia cells is error-prone, especially in regions close to  $A\beta$ -plaques, where microglia cells are densely packed. This problem was tackled by starting with the identification of the microglia's soma. This part of the microglia cells should overlap with its nucleus and shows high intensity values, making it easily discernible. Segmentation of microglia nuclei and somas was performed using a customized level-set-based cell segmentation method [19]. The main algorithm parameters are the weight for the energy terms minimizing the perimeter ( $\nu$ ) and the area ( $\mu$ ), which are empirically selected for each segmentation task. Larger parameter values correspond to smoother segmentation results. For the microglia nucleus segmentation, the DNA component image was used as input, and level-set parameters were set to  $\nu=2$  and  $\mu=3$ . Similarly, for the microglia soma segmentation the summation of the intensity values of the membrane (TMEM, PRY12, FTL, Iba) component images was utilized as input and level-set parameters were set to  $\nu=2$  and  $\mu=3$ . In both cases, level-sets were initialized with regions obtained using the Otsu thresholding method [20] which is robust to intensity variation between images originating from the white and grey matter. Additionally, somas and nuclei with a total area smaller than 50 and 30 pixels, respectively, were removed.

For the extension of the obtained segmentation to the whole cytoplasmic area, the approach previously described for soma was repeated with less strong regularization ( $\nu=2$ ,  $\mu=2$ ). The result of this step was a finer segmentation capturing microglia areas that are less bright than the soma. Connected components overlapping with the previously identified somas were regarded as microglia cells, whereas not overlapping components were considered as possible detached processes. At this step, in case a blood vessel was identified in an image, the Li thresholding method [21] was chosen over Otsu for the initialization of the level-sets algorithm, as it is less sensitive to the high intensity pixels representing the vessel. Vessels were defined as components larger than 4000 pixels, after Otsu thresholding of the autofluorescent component image.

For correct identification of microglia cells in the proximity of  $A\beta$ -plaques, the watershed segmentation was applied specifically to those cells whose cytoplasmic area is shared among multiple microglia somas [22].  $A\beta$ -plaque identification was performed employing a semi-supervised approach using Ilastik [23].

Finally, branches identified within a 10 pixel radius from the region corresponding to each identified

microglia soma were identified as detached processes and assigned to the microglia cell.

A sample resulting segmentation of entire microglial cells is illustrated in Additional file 1: Fig. S2e. For the evaluation of our algorithm, 186 cells were manually segmented, in 7 images from different subjects and regions. Our proposed segmentation framework outperformed the available segmentation solutions correctly capturing 153 cells (Inform: 12 cells, Abdolhoseini et al., 2019: 49 cells compare Additional file 1: Fig. S2g), with false positive 33 cells (Additional file 1: Fig. S2h) and false negatives 40 cells (Additional file 1: Fig. S2i). Among the correctly identified cells, median Dice's similarity index [24] of 0.8 was achieved (Additional file 1: Fig. S2f).

### Cell phenotype identification

Superimposing the segmentation masks onto the component image of all membrane markers, four mean intensity values were extracted for each cell. Afterwards, intensity values were normalized imposing Z-score transformation. For the definition of the different microglia cell types Phenograph [25], an unsupervised clustering method, was utilized. For Phenograph 100 nearest neighbours along with the default parameters were selected, in order to avoid overclustering due to the limited amount of markers. Subsequently, for each Phenograph identified cluster the variability of the single-cell marker expression values was examined (Additional file 1: Fig. S3) through a violin plot [26] indicating the variation in each cluster, in parallel with their expression patterns as illustrated in the composite images.

### Analysis of cellular phenotypes

The median expression value of each marker for each phenotype was illustrated with a heatmap. The similarities among the identified phenotypes were observed from a t-SNE [27] embedding using the same input as in Phenograph and the default parameters. The t-SNE embedding was coloured according to the cluster of each cell, its cohort or its individual marker expression values [28].

To explore the differences between the Alzheimer patients and controls regarding their phenotypes and their spatial relationship with the A $\beta$ -plaques, an interactive, data-driven pipeline described by [29] was utilized. First, using a version of raincloud plots [29] the phenotypes that exist predominantly in each cohort are identified and consequently, their relative position regarding the A $\beta$ -plaques using a visual query system are explored. For the exploration of the variability in each subject and the validation of our findings, a customized version of the motif glyphs described in our previous work [30] was employed.

### Statistical analysis

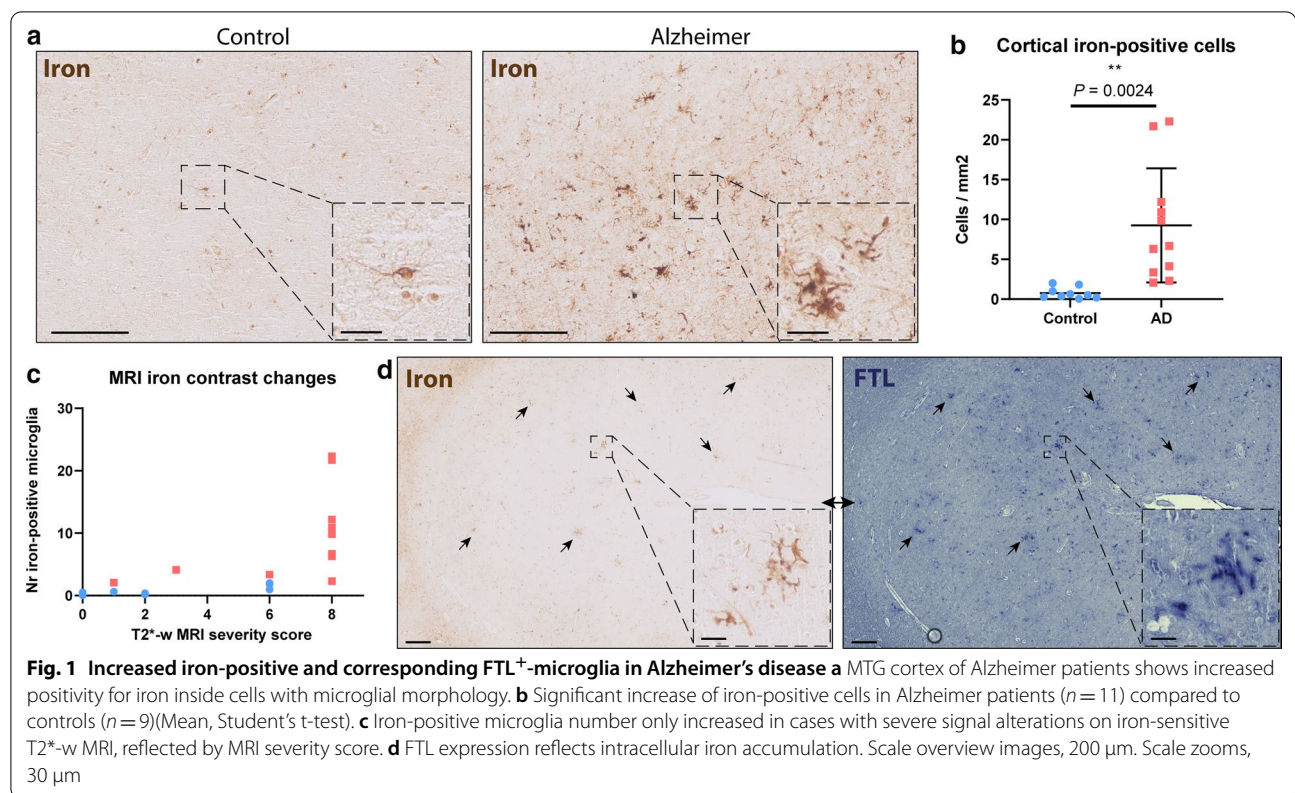
Firstly, variables were inspected for being gaussian distributed. If normally-distributed, data plots represent the mean and the standard deviation. For not normally-distributed data, data plots show the median with the corresponding interquartile range. Comparison of two continuous variables was performed using a two-tailed unpaired Student's independent t-test (normally-distributed) or a Mann–Whitney U test (not normally-distributed). Paired normally distributed data were analysed using a two-tailed paired Student's t-test. Bonferroni post-hoc analysis was performed, and a significance level of  $P < 0.05$  was used. The linear correlation between identified number of cells and different pathological hallmarks was assessed using the Pearson correlation coefficient. All statistical tests were performed using GraphPad Prism (Version 8.00, La Jolla, San Diego, CA, USA).

## Results

### FTL<sup>+</sup>-microglia reflect iron accumulating microglia in Alzheimer's disease

An enhanced Perl's staining for iron revealed an abundance of iron-positive cells in the cortex of the MTG in Alzheimer's patients. On further inspection, iron-positive cells showed characteristic microglia morphology with a small soma and many thin processes (Fig. 1a) and quantification indicated a significant increase of iron-positive cells in Alzheimer patients compared to controls ( $P = 0.0024$ ; Fig. 1b). Additionally, iron-positive cells appeared to cluster in groups, something that was not observed in control patients (Fig. 1a). All MTG tissue blocks have also previously been scanned using T2\*-w MRI, sensitive for paramagnetic substances such as iron. MRI images were scored based on alterations in signal intensity reflecting overall parenchymal iron accumulation and focal iron depositions, and were published by Bulk et al. [10]. An increase of iron-positive microglia appeared to be only present in cases with the highest MRI severity score, indicating a significant increase of iron-positive microglia only to occur in subjects with a pronounced macroscopic iron-phenotype (Fig. 1c). Subsequently we studied the correspondence of iron accumulation with altered expression of the main iron-storage protein ferritin light chain (FTL), as FTL is known to be expressed in microglia and oligodendrocytes, whereas heavy chain ferritin is primarily expressed by neurons in Alzheimer tissue [31]. The Perl's staining and the FTL staining showed a highly similar staining pattern, with focal clusters of cells representing microglia morphology (Fig. 1d). Thus, increased expression of the main iron-storage protein FTL appears to reflect iron accumulation in microglial cells.

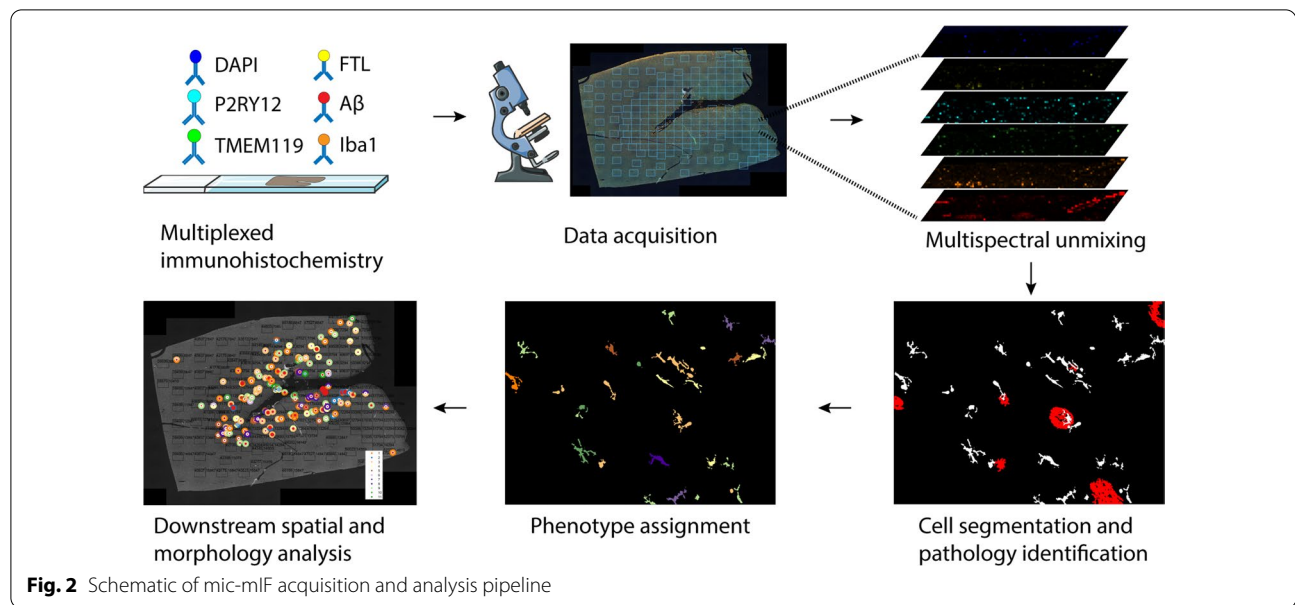




**Quantitative analysis enables microglia phenotyping**

To confirm the microglial origin of FTL<sup>+</sup> cells, study their activation state and potential interaction with A $\beta$ , we designed the microglia multispectral immunofluorescence (mic-mIF) panel that can simultaneously detect 6 different markers (Additional file 1: Table S2). The MTG of 12 Alzheimer patients, both of early- and late onset, and 9 control subjects (Additional file 1: Table S1) was stained and imaged. After image acquisition and multispectral unmixing of the data, images were exported for automated segmentation, phenotyping and spatial analysis (Fig. 2). In total, 3149 images (110–236 per subject) were obtained. Multispectral unmixing allowed for simultaneous detection of FTL with the nuclear marker DAPI, TMEM119, P2RY12, Iba1 and A $\beta$  at 0.5  $\times$  0.5  $\mu$ m resolution (Fig. 3a). TMEM119 and P2RY12 are generally considered homeostatic microglia-specific markers, based on transcriptomic [3, 32], in vitro [33–35] and post-mortem IHC studies [35–37], whose expression decreases when activated. Iba1, on the other hand, is a pan microglia/macrophage marker, which is upregulated upon activation. Finally A $\beta$  stains the characteristic pathological A $\beta$ -plaques that form in the parenchyma of Alzheimer patients. Images were segmented using a targeted in-house segmentation pipeline allowing segmentation of cells with processes (like microglia) in 2D images

(Fig. 3b; Additional file 1: Fig. S2). After segmentation, unsupervised clustering using Phenograph assigned single segmented cells to 20 separate clusters. Following manual evaluation of the unsupervised clusters, 6 clusters were excluded based on non-microglial morphology and/or sub-threshold expression of all microglial markers (TMEM119/P2RY12/Iba1). In addition, three times two clusters were merged based on similarity in protein expression levels and their visual appearance (Additional file 1: Fig. S3). Exclusion of the non-microglial cells resulted in identification of 69,227 cells, with no significant differences in the number of microglia per mm<sup>2</sup> between control and Alzheimer patients in either grey matter (GM) or white matter (WM) (Fig. 3c). The remaining 11 clusters (C1–C11) were identified as major microglia phenotype clusters (Fig. 3d). Though the 11 different phenotypes clustered on the t-SNE plot, the low degree of separation suggests a rather continuous spectrum of expression of the microglia markers (Fig. 3e). The control and Alzheimer patients did cluster together, and the marker-based t-SNE plots already revealed more cells with high TMEM119 and P2RY12 expression in controls, but increased FTL expression in Alzheimer patients (Fig. 3f). With regard to anatomical region, only C1 and C2 appeared to be more present in the grey matter (GM), whereas C5 and C6 appeared



to be proportionally more present in the white matter (WM) (Fig. 3g). Four FTL<sup>+</sup> clusters (C1–C3, C5) were identified, with differing expression levels and co-expression levels of P2RY12, TMEM119 and Iba1 (Fig. 3d). Cluster C1 (FTL<sup>+</sup>Iba1<sup>+</sup>) appeared significantly more present in Alzheimer patients ( $P=0.0264$ ), while C2 (P2RY12<sup>+</sup>TMEM119<sup>+</sup>FTL<sup>+</sup>Iba1<sup>+</sup>) was more present in controls ( $P=0.0055$ ; Fig. 3h). FTL<sup>+</sup>Iba1<sup>+</sup> clusters lacking either P2RY12 (C3) or TMEM119 (C5) did not differ significantly in prevalence between control and Alzheimer patients. Cluster C4 showed solely Iba1 expression, meaning that this cluster likely also consists of non-resident infiltrating macrophages. Additionally, three P2RY12<sup>+</sup> clusters (C6–C8) were identified, with the highest expressing cluster (C8) being more present in controls. The same applied for the TMEM119<sup>+</sup> clusters (C9–C11), with C10 and C11 having higher expression and being more present in control patients. These results indicate a small shift of homeostatic microglia positive for P2RY12 and TMEM119 in controls towards activated microglia, with downregulated expression of P2RY12 and TMEM119 in Alzheimer patients. In addition, a specific

Alzheimer-associated cluster shows increased expression of a combination of FTL and Iba1.

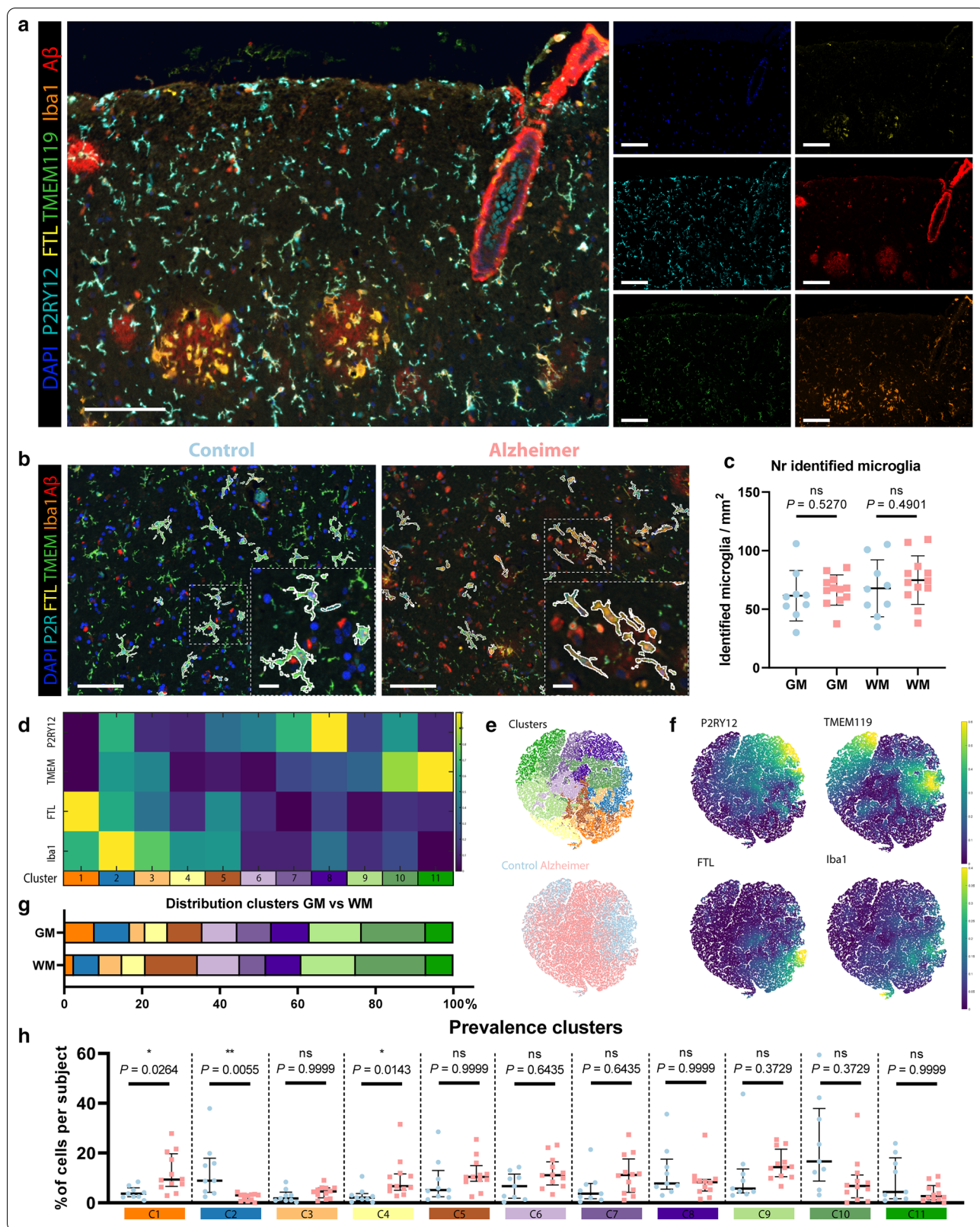
### Spatial analysis of FTL<sup>+</sup> microglia clusters

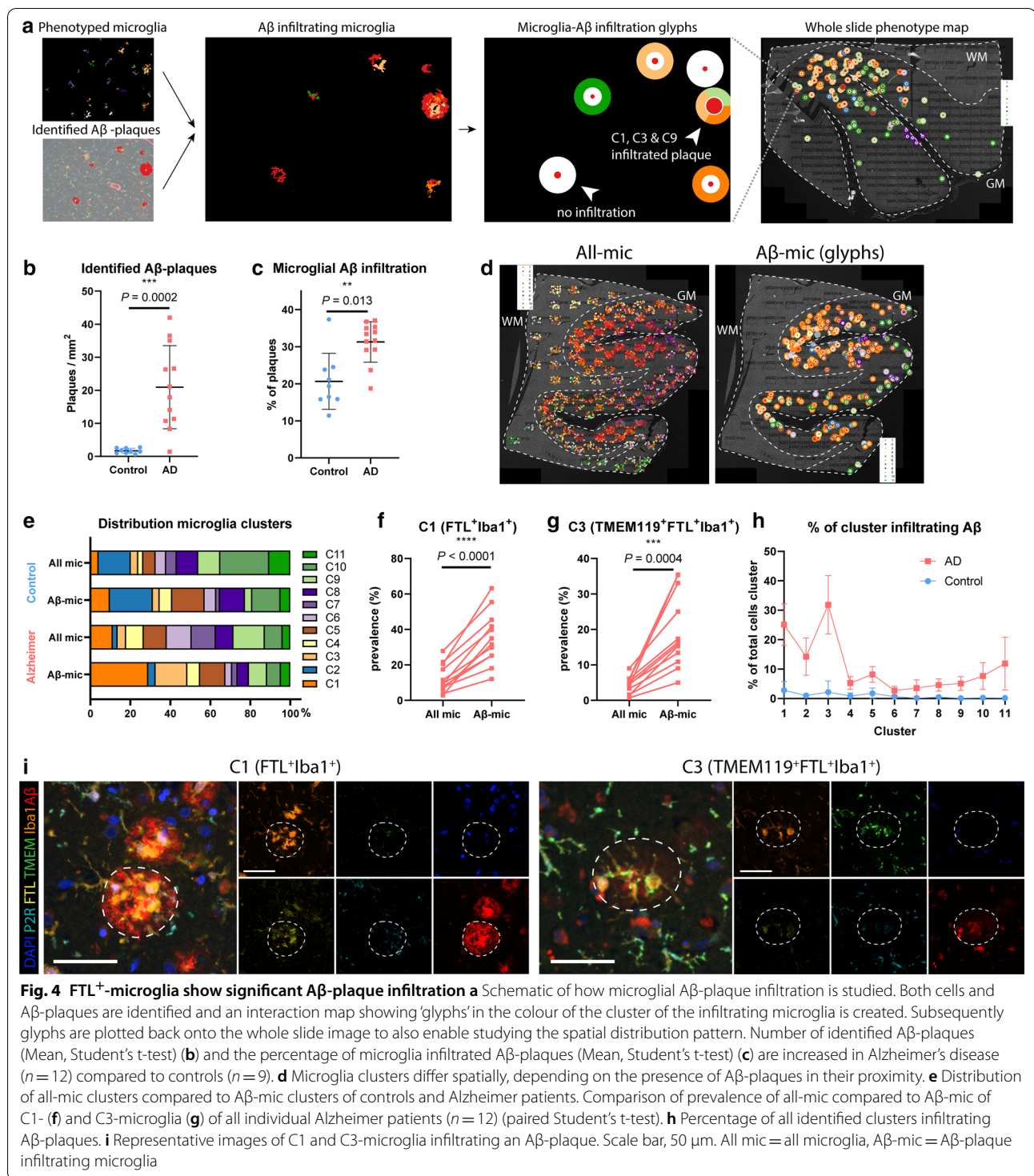
After cell phenotype identification, all microglia were assessed for proximity to parenchymal Aβ-plaques. For visualization purposes, a second image was created, where infiltrated Aβ-plaques were plotted onto the original image as a ‘glyph’ (Fig. 4a) [30], with the different colours corresponding to the respective cluster of the infiltrating microglia, to analyse which clusters predominantly infiltrated Aβ-plaques. Subsequently, all individual cells represented as cluster-colored dots or the cluster-colored glyphs were plotted back onto the original whole slide image (Fig. 4a), to assess differences in cluster composition of microglial Aβ infiltration on a whole-section scale. As expected, quantification showed significantly more identified Aβ-plaques in Alzheimer patients, although some were found in controls as well ( $P=0.0002$ ; Fig. 4b). Furthermore, a higher percentage of the plaques showed microglia infiltration in Alzheimer patients ( $P=0.013$ ; Fig. 4c). Looking at the whole slide distribution, Aβ-plaques

(See figure on next page.)

**Fig. 3** Identification of homeostatic and activated Alzheimer-associated microglia clusters **a** Example of mIF image of an Alzheimer patient. **b** Exemplary images of segmented microglia in a control and an Alzheimer patient. **c** Number of identified cells in the GM and WM of controls (blue;  $n=9$ ) and Alzheimer patients (red;  $n=12$ ) (Mean, Student’s t-test). **d** Heatmap showing the expression of the four different markers (P2RY12, TMEM119, FTL and Iba1), in the 11 identified microglia clusters. **e** t-SNE plot of all individual cells showing the distinct colour-coded clusters and of control- vs. Alzheimer-patient-derived cells. **f** t-SNE plots colour-coded for intensity of the four individual markers. **g** Distribution of clusters in GM and WM. **h** Prevalence of identified clusters (C1–C11) in individual control (blue;  $n=9$ ) and Alzheimer patients (red;  $n=12$ ) (Median, Mann–Whitney U test). Scale bar, 100  $\mu\text{m}$ . Scale bar zooms, 20  $\mu\text{m}$ . GM Grey matter, WM White matter



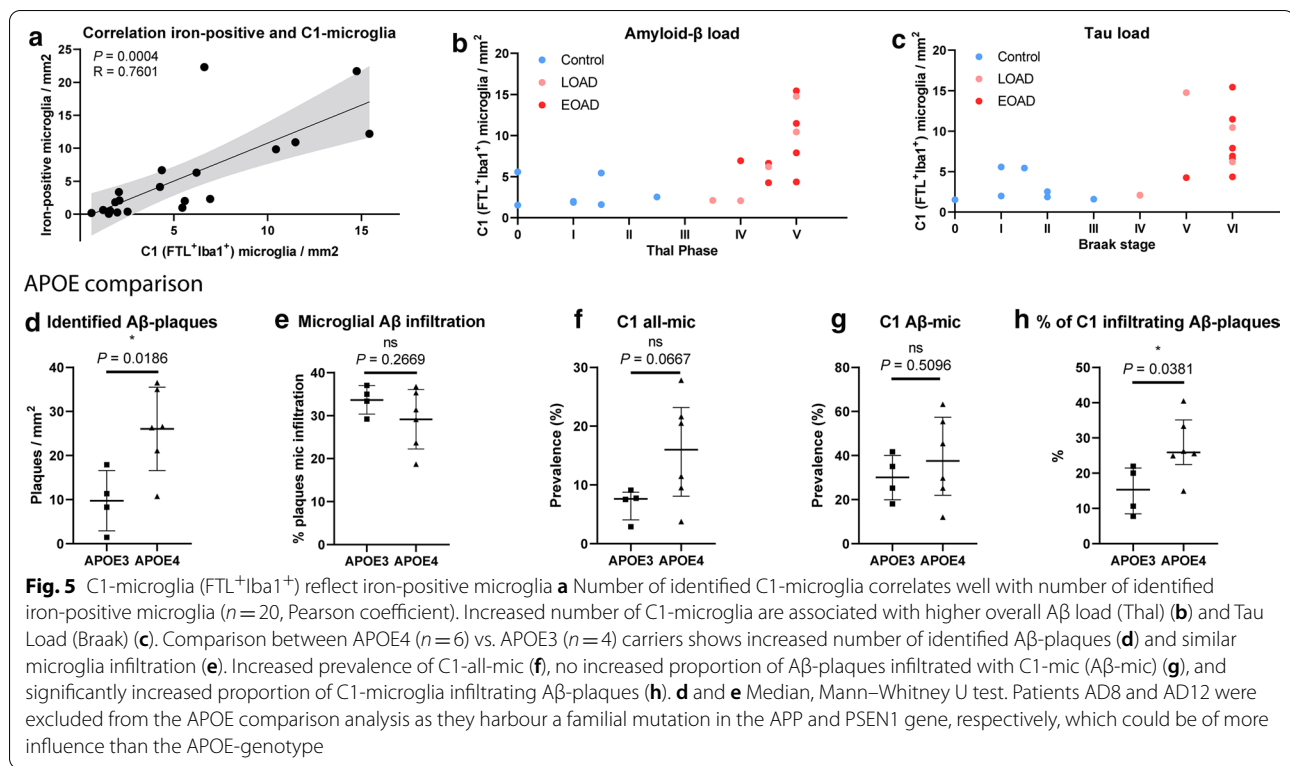




were found to be more present in the coronal sulcus rather than the gyrus. This also appeared to be associated with the regional microglia phenotype, as can be seen for the predominantly purple (C6–C8) microglia populating the Aβ-plaque deplete regions (Fig. 4d).

To quantify the influence of Aβ-plaques on microglia phenotype, we compared all phenotyped microglia (all-mic) with the subset of microglia infiltrating Aβ-plaques (Aβ-mic). Controls showed a slight percentage increase of C1 and C5 in Aβ-mic compared to

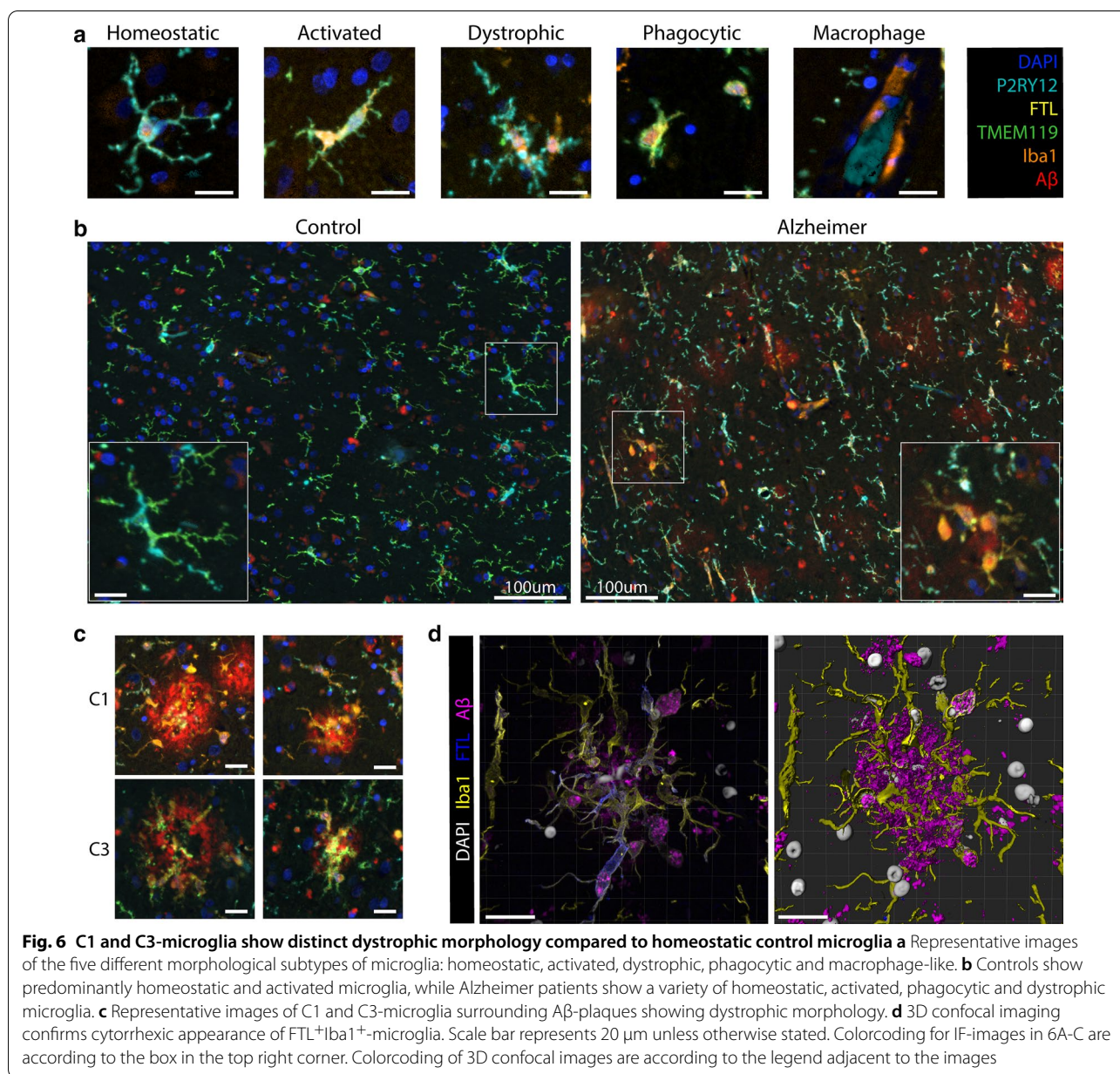




all-mic, and less A $\beta$ -plaque infiltration of TMEM119<sup>+</sup> clusters C9–C11 (Fig. 4e), though this was based on a limited total number of A $\beta$ -plaques. Alzheimer patients on the other hand, showed a large percentual increase of FTL<sup>+</sup>-clusters C1 and C3 in the A $\beta$ -mic population (Fig. 4e), which was also statistically significant when looking at subject-specific proportional increases (C1:  $P < 0.0001$ , C3:  $P = 0.0004$ ; Fig. 4f, g). While C1 and C3-microglia together make up less than 20% of all-mic, they constitute almost 50% of the A $\beta$ -mic population (Fig. 4e). P2RY12<sup>+</sup> clusters C6–C8, on the other hand, showed a small contribution to A $\beta$ -mic compared to all-mic (Fig. 4e). Finally, not only did C1 and C3 make up the majority of A $\beta$ -mic, but also when examining the proportions of these individual clusters that directly infiltrated A $\beta$ -plaques, they showed much higher proportion of infiltration than all the other clusters (Fig. 4h). A visual example of the C1 and C3-microglia infiltrating an A $\beta$ -plaque on the original mic-mIF images can be found in Fig. 4i. All in all, these results suggest A $\beta$ -plaques to be predominantly infiltrated by a specific subset of microglia, characterized by increased FTL and Iba1 expression and loss of expression of homeostatic markers P2RY12 or TMEM119 and P2RY12.

### Correlation of FTL<sup>+</sup>-microglia with pathology

As already shown in Fig. 1d, FTL staining closely followed the enhanced Perl's staining showing microglial iron loading. Therefore, we also checked the correlation of the number of iron-positive microglia with the number of identified microglia of different FTL<sup>+</sup> clusters. The number of identified C1 (FTL<sup>+</sup>Iba1<sup>+</sup>) microglia correlated well with number of iron-positive-cells ( $R = 0.7601$ ,  $p = 0.0004$ ; Fig. 5a), while other FTL<sup>+</sup> clusters with lower expression (C2, C3) did not show correlation with number of iron-positive cells (Additional file 1: Fig. S4a, d). This suggests that it is especially the marked increase of FTL expression found in C1-microglia that reflects substantial iron loading, while moderate FTL expression is also found in non-iron accumulating cells in controls. Although we already found C1-microglia to significantly infiltrate A $\beta$ -plaques, we also checked for its correlation with overall A $\beta$  and Tau load, as assessed by a neuropathologist using Thal stage and Braak stage, respectively. A marked increase of the number of C1-microglia was solely found in high-pathology load subjects with Thal phase V, and Braak stage V/VI (Fig. 5b, c), though not all high-pathology load subjects show increase of C1-microglia. C2-microglia were primarily found in controls with low Braak stage I/II and Thal I-II, whereas C3-microglia were present in both controls and Alzheimer patients



with varying pathological burdens (Additional file 1: Fig. S4b, c, e, f). This is in line with the finding that iron-positive microglia were particularly present in Alzheimer patients with advanced iron loading. However, there is lack of Alzheimer patients with intermediate Thal- and Braak-scores, making it impossible to state that an increase of C1-microglia is exclusive to advanced stage disease, and C3 represents an intermediate state between C2 in controls and C1 in advanced disease. Further investigation into the differences between early-onset Alzheimer’s disease (EOAD, onset < 65y) patients and late-onset Alzheimer’s disease (LOAD, onset > 65y) patients,

showed no differences in Aβ load, microglia prevalence, or Aβ-infiltration of C1, C2 nor C3 (Additional file 1: Fig. S4g–q). In addition, we looked at differences between APOE3 and APOE4 carriers, as the latter have been found to have elevated ferritin levels in the CSF [38]. As expected, APOE4 carriers had more Aβ-plaques (Fig. 5d), but did not show overall increased microglia infiltration (Fig. 5e). Though sample sizes for both groups were small ( $n=4-6$ ), a trend indicating higher prevalence of C1-microglia in the GM could be observed ( $P=0.0667$ ; Fig. 5f), which was not the case for C2 and C3-microglia (Additional file 1: Fig. S4r, s) However, no difference was

observed when looking at the proportion of A $\beta$ -plaques infiltrated by C1-microglia (A $\beta$ -mic) ( $P=0.5096$ ; Fig. 5g). This suggests that even though a higher percentage of C1-microglia infiltrate A $\beta$ -plaques ( $P=0.0381$ ; Fig. 5h), this is likely due to the increased number of A $\beta$ -plaques present in the APOE4 carriers.

#### **FTL<sup>+</sup>Iba1<sup>+</sup>-microglia have a dystrophic morphological appearance**

Finally, we visually evaluated the morphological appearance of all phenotyped microglia in the same dataset, as this provides additional information about the activation stage of the microglia. Two authors (BK and LdH), evaluated the cells according to five distinctive morphological clusters: homeostatic, activated, dystrophic, phagocytic and perivascular macrophages (Fig. 6a), based on previously described morphological phenotypes [39]. The parenchyma of controls was predominantly populated by C6–C11-microglia, which consistently expressed TMEM119 and/or P2RY12. These cells presented with homeostatic morphology, showing small circular or oval cell bodies, with thin highly ramified processes and extensive branches (Fig. 6b). Morphological appearance therefore appeared to be in line with the homeostatic protein phenotype. Occasionally activated microglia were identified, which have larger cell bodies and noticeably fewer branches and ramifications (especially second degree) (Fig. 6a). Activated cells generally showed higher Iba1 and FTL expression and were often phenotyped as C2-microglia (Fig. 6a). Microglia in Alzheimer patients, on the other hand, had a much more heterogeneous appearance; homeostatic, activated, dystrophic and phagocytic microglia could all be observed within the coronal sulcus of a single patient (Fig. 6b). Though almost all phenotype clusters and morphological clusters could be observed, we focussed on the C1-microglia, as they reflected iron-positive microglia. We found the striking majority of C1-microglia to have a dystrophic morphological appearance. The dystrophic cells show a very distinct phenotype, often with a cloudy or cytorrhetic (fragmentation of the cytoplasm) appearance which results in ill-defined processes (Fig. 6a). There is often deramification and the remaining branches show spheroids and fragmentation. Especially microglia (both C1 and C3) infiltrating A $\beta$  plaques showed highly dystrophic morphological characteristics, indicative of an advanced activated/neurodegenerative state (Fig. 6c). The dystrophic morphology was also verified using 3D confocal microscopy, which also showed the same cytorrhetic appearance of microglia surrounding the A $\beta$ -plaques (Fig. 6d). All in all, the finding of a dystrophic phenotype in C1-microglia was in line with the increased Iba1 and decreased TMEM119 and P2RY12 expression, which

accompanied the pronounced FTL expression. They also reflected the morphological appearance of the iron-positive microglia identified on the Perl's staining (Fig. 1a).

#### **Discussion**

In this manuscript, we confirmed that increased FTL expression reflects an increase in iron accumulation in microglia in the cortex of Alzheimer patients. Microglia with increased FTL expression also showed higher Iba1 expression, but loss of homeostatic markers TMEM119 and P2RY12, indicative of an activated phenotype. On further investigation this FTL<sup>+</sup>Iba1<sup>+</sup> phenotype appeared to be increasingly present in Alzheimer patients and the predominant A $\beta$ -plaque infiltrating microglia phenotype. Morphologically they appeared to be in a dystrophic activation stage.

Firstly, in this study we confirmed that previously identified iron-positive cells in Alzheimer patients [40, 41] are of microglial rather than astrocytic origin, and show high FTL expression. Subsequently, using multispectral fluorescence and unsupervised clustering, we identified several FTL<sup>+</sup>-clusters, which were variably present in controls and Alzheimer disease stages. C2-microglia, which displayed positivity for all included microglia markers, were almost exclusively present in control patients. Conversely, C1-microglia (FTL<sup>+</sup>Iba1<sup>+</sup>) were significantly more present in AD patients, and C3-microglia (TMEM119<sup>+</sup>FTL<sup>+</sup>Iba1<sup>+</sup>) were marginally present in either group. Interestingly, both C1 and C3-microglia showed a strong tendency to infiltrate A $\beta$ -plaques. C1-microglia were almost exclusively present in advanced stage Alzheimer patients, whereas C2-microglia were primarily detected in controls (with low Thal/Braak stages), and C3-microglia were variably present across controls and Alzheimer patients of all stages. Regarding the temporal dynamics of these clusters, one could therefore hypothesize that in Alzheimer's disease microglia surround A $\beta$ -plaques and lose P2RY12 expression, as has been observed previously by others (transition from C2 to C3) [36, 42]. As of yet we do not know what the relevance is of the preserved TMEM119-expression. Over time, these microglia take up iron, causing a pronounced increase of FTL expression and loss of TMEM119. This corresponds to the fact that only C1-microglia appeared to correlate with iron-accumulating microglia. However, our study population is not ideal to dissect the temporal dynamics of these clusters, since the majority of Alzheimer patients showed advanced disease (Braak V/VI) and only two patients showed mild to moderate (Braak III/IV). Future work studying these phenotypes in a larger cohort with a larger range of disease stages would be highly relevant to accurately determine



at what stage of the disease C2-microglia prevalence decreases and C1 and C3-microglia prevalence increases.

Several qualitative studies had previously identified increased presence of dystrophic ferritin<sup>+</sup> microglia in brain tissue of Alzheimer patients [6, 40, 43, 44]. The dystrophic morphological appearance was also confirmed in this study, though the functional insights of these morphologically defined states remains debatable. Our spatial analysis revealed a strong tendency of FTL<sup>+</sup>Iba1<sup>+</sup> to infiltrate A $\beta$ -plaques; significantly more than can be expected based on prevalence of the cluster itself, and more than any other identified microglia cluster. Although some other studies had already looked into the association of dystrophic ferritin<sup>+</sup> microglia with A $\beta$ -plaques [6, 7, 31, 40, 45], results were inconsistent, as none of these studies so far looked into the relative proportion of these microglia in the total population. The importance of this is also stressed in a recent study by Nguyen et al. [46], in which they found an amyloid-responsive microglia (ARM) subset, characterized by CD163, but did not pick up on the A $\beta$ -plaque-infiltrating properties of their identified ferritin<sup>+</sup> microglia. Finally, we were able to further characterize iron-positive/FTL<sup>+</sup>-microglia by analyzing co-expression of several other microglia markers on a single cell level. This revealed that C1-microglia, with the highest FTL protein expression and increased Iba1 expression, showed complete loss of expression of homeostatic markers TMEM119 and P2RY12. Although we acknowledge that our FTL<sup>+</sup>Iba1<sup>+</sup>(P2RY12<sup>-</sup>TMEM119<sup>-</sup>)-microglia were only characterized using four protein-markers, which is only a fraction compared to the total amount of genes used to define specific transcriptomic states such as the DAM/HAM-states, we do want to highlight the similarities. The DAM/HAM-subsets showed FTL among the highest upregulated genes, with coinciding downregulation of TMEM119 and P2RY12 [3, 4]. Additionally clustering around A $\beta$ -plaques was also reported as a characteristic feature of DAM microglia [3], as is observed for the identified FTL<sup>+</sup>Iba1<sup>+</sup>-microglia.

To date, the reason for the observed increase of FTL-expression remains disputed. With FTL being the long-term storage component of ferritin, its expression is likely to be increased in response to increased intracellular labile iron concentrations. Yet, ferritin is also widely recognized as an acute phase reactant and it has also been suggested that microglia upregulate ferritin as a response to exhaustion, caused by the attempt to phagocytose aggregated A $\beta$  [45]. However, our findings show that the identified FTL<sup>+</sup>Iba1<sup>+</sup>-microglia closely reflected microglia with high levels of the metal iron, and therefore suggest that the observed increased FTL-expression at least does not merely reflect inflammatory activation or

exhaustion, but also increased iron levels. This is in line with a previous study, which found ferritin levels in the CSF to not be associated with an inflammatory response in Alzheimer patients and hypothesized ferritin levels to rather reflect changes in iron associated with tangle and plaque pathology [47].

Why iron increases with age and even more profoundly in neurodegenerative diseases is still largely unknown [8, 48]. It is hypothesized to be caused by several factors including increased blood-brain barrier permeability and disorganization of the iron-dense myelin sheaths [49–51]. Alongside a general increase of iron in the parenchyma, iron was also shown to accumulate inside A $\beta$ -plaques [51, 52]. Therefore, a possible hypothesis for why iron is sequestered in microglia surrounding A $\beta$ -plaques, could be that the iron is taken up as byproduct while attempting to phagocytose the A $\beta$  aggregates. Conversely, considering we only found approximately 25% of iron-accumulating C1-microglia to infiltrate A $\beta$ -plaques, iron is more likely sequestered using either DMT1 or Transferrin-receptors and stored inside FTL, in an attempt to mitigate the potentially toxic effects of free iron, which in its free form is suggested to partake in Fenton's reaction to form hydroxyl radicals and cause toxic oxidative stress [50]. When iron is taken up by microglia, it first becomes part of the labile iron pool, where it can produce reactive oxygen species damaging the mitochondria and other cell organelles [53]. Studies performed using peripheral tissue cells showed the non-CNS equivalent of microglia, macrophages, to respond to intracellular iron accumulation by also activating the NLRP3 inflammasome [54]. Accordingly, *in vitro* and *in vivo* studies have shown that exposure to a combination of iron and A $\beta$  induces the production of cytokine IL-1 $\beta$  and a switch to glycolytic metabolism in microglia, both of which can be interpreted as NLRP3-inflammasome activation [55, 56]. NLRP3-inflammasome activation in microglia was shown to be able to modify disease progression in two different Alzheimer mouse models [57, 58]. Our data support the *in vitro* and mouse model evidence that iron and A $\beta$  can act together to accelerate disease progression via microglial inflammasome activation, by showing that in human brain tissue of Alzheimer patients, microglia are exposed to a combination of iron and A $\beta$ . Finally, these findings are also in line with recent clinical studies, in which iron was found to act as a potential disease modifier by accelerating deterioration in Alzheimer patients with high A $\beta$  load [12, 13].

Thanks to the possibility to visualize up to six protein markers on the same section using mIF, we could better study the great heterogeneity in microglia phenotype and its spatial relationship with pathology. A limitation of mIF compared to other high-dimensional techniques



such as single-cell or imaging mass cytometry is the limited number of markers available to characterize the complex microglial activation states. However, single-cell mass cytometry lacks the spatial component, which is essential when studying the relation with A $\beta$ . Imaging mass cytometry, on the other hand, does capture the spatial distribution, however to date does not enable high-throughput analysis and offers limited resolution. Since microglia have very complicated and variable morphology, solely evaluating protein expression directly surrounding the nucleus is insufficient, and high-resolution images are required for proper segmentation and phenotyping. Secondly, as we are studying relatively rare activated microglia subtypes that will not be present in every ROI or even subject, we required high-throughput quantitative analysis methods. The mIF-mic panel, together with our optimized microglia segmentation pipeline for 2D-images, enabled accurate segmentation and analysis of >60,000 cells to carefully identify the FTL<sup>+</sup>-microglia in an unbiased fashion.

In this study, we adopted an unsupervised learning approach to generate distinct clusters in our dataset, and avoid bias in the identification in clusters, as can be present in more classical IHC studies. However, as already indicated in the results section, even though distinct clusters were identified, the low degree of separation on the t-SNE mapping and similarity on the associated heatmap, suggest these clusters may be more of a continuum rather than distinct subsets. This is in line with other transcriptomic and proteomic studies, in which they also showed the microglia clusters to be more of a continuum, even when studying substantially more genes or proteins [5, 59, 60]. However, employment of distinct clusters allows for studying the extreme ends of the continuum of the clusters to find meaningful changes in activation state. Finally, to verify that we were not looking at arbitrary differences in expression levels, we visually checked distinguishability of all independent clusters on the associated immunohistochemical images and merged clusters where this was not possible, as illustrated in Additional file 1: Fig. S3.

Future studies looking into the effect of iron and A $\beta$  in humanized models such as iPSC-derived microglia would be extremely valuable to decipher the functional effect of this combination, and the influence of Alzheimer-associated genetic risk variants such as APOE. In addition, since microglia, as well as iron accumulation, are shown to be involved in many different neurodegenerative and neuro-immunological disease such as Parkinson's disease and multiple sclerosis, it would be worthwhile looking into this interaction as a common pathway in neurodegeneration. Like for Alzheimer disease, iron could interact with the accumulating protein of interest to affect

microglia functioning and consequentially accelerate disease progression.

## Conclusion

In summary, we showed that our multispectral immunofluorescence pipeline allowed for accurate identification of specific microglia clusters, and more importantly for the spatial analysis with respect to pathological hallmarks. In this specific study we identified dystrophic FTL<sup>+</sup>Iba1<sup>+</sup>TMEM119<sup>-</sup>P2RY12<sup>-</sup>-microglia to be significantly more present in Alzheimer's disease patient, and to be the predominant A $\beta$ -plaque infiltrating microglia cluster. Finally, in correspondence with the increase of FTL-expression, FTL<sup>+</sup>Iba1<sup>+</sup>-microglia showed massive iron-loading.

## Supplementary Information

The online version contains supplementary material available at <https://doi.org/10.1186/s40478-021-01126-5>.

### Additional file 1.

## Acknowledgements

We would like to thank all patients who donated their brain to the Leiden University Medical Center (LUMC), Netherlands Brain Bank (NBB) or the Normal Aging Brain collection Amsterdam (NABCA), and prof. A.J.M. Rozemuller for neuropathological evaluation of the brains. We would also like to thank I.M. Hegeman-Klein for technical assistance with histological and immunohistochemical techniques.

## Author contributions

B.K. and L.v.d.W. conceived and designed the project. B.K., M.I. and N.F.C.d.M. designed the antibody panel for microglia multispectral immunofluorescence (mic-mIF). A.S., O.D. and B.K. created the microglia segmentation pipeline. A.S. created the spatial analysis tools for mic-mIF data under supervision of B.P.F.L., J.D. and T.H.. B.K. and L.d.H. performed morphological evaluation of microglia. B.K. and A.S. analysed and interpreted the mic-mIF data. B.K., A.S., W.M.C.v.R-M, T.H., and L.v.d.W. wrote the manuscript. All authors read and approved the final manuscript.

## Funding

B.K. is supported by an MD/PhD-grant from the Leiden University Medical Center. In addition, he has received funding from an early career fellowship from Alzheimer Nederland (WE.15-2018-13) and a Eurolife Scholarship for Early Career researcher. A.S. has received funding through Leiden University Data Science Research Programme. LvdW received funding from The Netherlands Organization for Scientific Research (NWO) Innovational Research Incentives Scheme (MDI 864.13.014).

## Availability of data and materials

The data that support the findings of this study are available from the corresponding author upon reasonable request.

## Competing interests

The authors have no conflicts of interest to declare. All co-authors have seen and agree with the contents of the manuscript and there is no financial interest to report.

## Consent for publication

Not applicable.

**Ethics approval and consent to participate**

All material has been collected with written consent from the donors and the procedures have been approved by the Medical Ethical committee of the LUMC and the Amsterdam UMC.

**Author details**

<sup>1</sup> Department of Human Genetics, Leiden University Medical Center, Albinusdreef 2, 2333 ZA Leiden, The Netherlands. <sup>2</sup> Department of Radiology, Leiden University Medical Center, Leiden, The Netherlands. <sup>3</sup> Department of Pathology, Leiden University Medical Center, Leiden, The Netherlands. <sup>4</sup> Department of Intelligent Systems, Delft University of Technology, Delft, The Netherlands. <sup>5</sup> Department of Cell and Chemical Biology, Leiden University Medical Center, Leiden, The Netherlands.

Received: 21 December 2020 Accepted: 30 January 2021

Published online: 17 February 2021

**References**

- Jansen IE, Savage JE, Watanabe K, Bryois J, Williams DM, Steinberg S et al (2019) Genome-wide meta-analysis identifies new loci and functional pathways influencing Alzheimer's disease risk. *Nat Genet* 51:404–413
- Lambert JC, Ibrahim-Verbaas CA, Harold D, Naj AC, Sims R, Bellenguez C et al (2013) Meta-analysis of 74,046 individuals identifies 11 new susceptibility loci for Alzheimer's disease. *Nat Genet* 45:1452–1458
- Keren-Shaul H, Spinrad A, Weiner A, Matcovitch-Natan O, Dvir-Szternfeld R, Ulland TK et al (2017) A unique microglia type associated with restricting development of Alzheimer's disease. *Cell* 169(1276–1290):e17
- Mathys H, Davila-Velderrain J, Peng Z, Gao F, Mohammadi S, Young JZ et al (2019) Single-cell transcriptomic analysis of Alzheimer's disease. *Nature* 570:332–337
- Zhou Y, Song WM, Andhey PS, Swain A, Levy T, Miller KR et al (2020) Human and mouse single-nucleus transcriptomics reveal TREM2-dependent and TREM2-independent cellular responses in Alzheimer's disease. *Nat Med* 26:131–142
- Lopes KO, Sparks DL, Streit WJ (2008) Microglial dystrophy in the aged and Alzheimer's disease brain is associated with ferritin immunoreactivity. *Glia* 56:1048–1060
- Grundke-Iqbal I, Fleming J, Tung YC, Lassmann H, Iqbal K, Joshi JG (1990) Ferritin is a component of the neuritic (senile) plaque in Alzheimer dementia. *Acta Neuropathol* 81:105–110
- Damulina A, Pirpamer L, Soellradl M, Sackl M, Tinauer C, Hofer E et al (2020) Cross-sectional and longitudinal assessment of brain iron level in Alzheimer disease using 3-T MRI. *Radiology* 296:192541
- Spotorno N, Acosta-Cabronero J, Stomrud E, Lampinen B, Strandberg OT, van Westen D et al (2020) Relationship between cortical iron and tau aggregation in Alzheimer's disease. *Brain* 143:1341–1349
- Bulk M, Kenkhuis B, van der Graaf LM, Goeman JJ, Natté R, van der Weerd L (2018) Postmortem T2\*-weighted MRI imaging of cortical iron reflects severity of Alzheimer's disease. *J Alzheimer's Dis* 65:1125–1137
- van Duijn S, Bulk M, van Duinen SG, Nabuurs RJA, van Buchem MA, van der Weerd L et al (2017) Cortical iron reflects severity of Alzheimer's disease. *J Alzheimer's Dis* 60:1533–1545
- Ayton S, Fazlollahi A, Bourgeat P, Raniga P, Ng A, Lim YY et al (2017) Cerebral quantitative susceptibility mapping predicts amyloid- $\beta$ -related cognitive decline. *Brain* 140:2112–2119
- Ayton S, Wang Y, Diouf I, Schneider JA, Brockman J, Morris MC et al (2019) Brain iron is associated with accelerated cognitive decline in people with Alzheimer pathology. *Mol Psychiatry* 66:1–10
- Braak H, Braak E (1991) Neuropathological staging of Alzheimer-related changes. *Acta Neuropathol* 66:239–259
- Braak H, Braak E (1995) Staging of Alzheimer's disease-related neurofibrillary changes. *Neurobiol Aging* 16:271–278
- Hyman BT, Phelps CH, Beach TG, Bigio EH, Cairns NJ, Carrillo MC et al (2012) National Institute on Aging-Alzheimer's Association guidelines for the neuropathologic assessment of Alzheimer's disease. *Alzheimer's Dement* NIH Public Access 8:1–13
- Ijsselstein ME, Brouwer TP, Abdulrahman Z, Reidy E, Ramalheiro A, Heeren AM et al (2019) Cancer immunophenotyping by seven-colour multispectral imaging without tyramide signal amplification. *J Pathol Clin Res* 5:3–11
- Abdolhoseini M, Kluge MG, Walker FR, Johnson SJ (2019) Segmentation, tracing, and quantification of microglial cells from 3D image stacks. *Sci Rep* 9:8557
- Dzyubachyk O, Van Cappellen WA, Essers J, Niessen WJ, Meijering E (2010) Advanced level-set-based cell tracking in time-lapse fluorescence microscopy. *IEEE Trans Med Imaging* 29:852–867
- Otsu N (1979) Threshold selection method from gray-level histograms. *IEEE Trans Syst Man Cybern SMC* 9:62–66
- Li CH, Lee CK (1993) Minimum cross entropy thresholding. *Pattern Recognit Pergamon* 26:617–625
- Beucher S, Lantuejoul C (1979) Use of watersheds in contour detection. *Int Work Image Process Real-Time Edge Motion Detect Rennes* 132:2.1–2.12
- Sommer C, Straehle C, Kothe U, Hamprecht FA (2011) Ilastik: interactive learning and segmentation toolkit. In: *Proceedings of the international symposium on biomedical imaging*, pp 230–233
- Dice LR (1945) Measures of the amount of ecologic association between species. *Ecology* 26:297–302
- Levine JH, Simonds EF, Bendall SC, Davis KL, Amir EAD, Tadmor MD et al (2015) Data-driven phenotypic dissection of AML reveals progenitor-like cells that correlate with prognosis. *Cell* 162:184–197
- Hintze JL, Nelson RD (1998) Violin plots: a box plot-density trace synergism. *Am Stat* 52:181–184
- Van Der Maaten L, Hinton G (2008) Visualizing data using t-SNE. *J Mach Learn Res* 9:2579–2605
- Höllt T, Pezzotti N, van Unen V, Koning F, Eisemann E, Lelieveldt B et al (2016) Cytosplasmic: interactive immune cell phenotyping for large single-cell datasets. *Comput Graph Forum* 35:171–180
- Somarakis A, Ijsselstein ME, Luk SJ, Kenkhuis B, de Miranda NFCC, Lelieveldt BPF et al (2021) Visual cohort comparison for spatial single-cell omics-data. *IEEE Trans Vis Comput Graph* 27:733–743
- Somarakis A, Van Unen V, Koning F, Lelieveldt BPF, Hollt T (2019) ImaCytE: visual exploration of cellular microenvironments for imaging mass cytometry data. *IEEE Trans Vis Comput Graph* 1:1
- Meadowcroft MD, Connor JR, Yang QX (2015) Cortical iron regulation and inflammatory response in Alzheimer's disease and APPSWE/PS1 $\Delta$ E9 mice: a histological perspective. *Front Neurosci* 9:255
- Krasemann S, Madore C, Cialic R, Baufeld C, Calcagno N, El Fatimy R et al (2017) The TREM2-APOE pathway drives the transcriptional phenotype of dysfunctional microglia in neurodegenerative diseases. *Immunity* 47:566–581
- Banerjee P, Paza E, Perkins EM, James OG, Kenkhuis B, Lloyd AF et al (2020) Generation of pure monocultures of human microglia-like cells from induced pluripotent stem cells. *Stem Cell Res* 49:102046
- Van Wageningen TA, Vlaar E, Kooij G, Jongenelen CAM, Geurts JGG, Van Dam AM (2019) Regulation of microglial TMEM119 and P2RY12 immunoreactivity in multiple sclerosis white and grey matter lesions is dependent on their inflammatory environment. *Acta Neuropathol Commun* 7:66
- Bennett ML, Bennett FC, Liddelov SA, Ajami B, Zamanian JL, Fernhoff NB et al (2016) New tools for studying microglia in the mouse and human CNS. *Proc Natl Acad Sci USA* 113:E1738–E1746
- Mildner A, Huang H, Radke J, Stenzel W, Priller J (2017) P2Y<sub>12</sub> receptor is expressed on human microglia under physiological conditions throughout development and is sensitive to neuroinflammatory diseases. *Glia* 65:375–387
- Zrzavy T, Hametner S, Wimmer I, Butovsky O, Weiner HL, Lassmann H (2017) Loss of "homeostatic" microglia and patterns of their activation in active multiple sclerosis. *Brain* 140:1900–1913
- Ayton S, Faux NG, Bush AI, Initiative ADN (2015) Ferritin levels in the cerebrospinal fluid predict Alzheimer's disease outcomes and are regulated by APOE. *Nat Commun* 6:6760
- Streit WJ, Xue QS, Tischer J, Bechmann I (2014) Microglial pathology. *Acta Neuropathol Commun* 2:1–17
- Connor JR, Menzies SL, St. Martin SM, Mufson EJ, (1992) A histochemical study of iron, transferrin, and ferritin in Alzheimer's diseased brains. *J Neurosci Res* 31:75–83
- Zeineh MM, Chen Y, Kitzler HH, Hammond R, Vogel H, Rutt BK (2015) Activated iron-containing microglia in the human hippocampus identified

- by magnetic resonance imaging in Alzheimer disease. *Neurobiol Aging* 36:2483–2500
42. Walker DG, Tang TM, Mendsaikhan A, Tooyama I, Serrano GE, Sue LI et al (2020) Patterns of expression of purinergic receptor P2RY12, a putative marker for non-activated microglia, in aged and Alzheimer's disease brains. *Int J Mol Sci* 21:66
  43. Kaneko Y, Kitamoto T, Tateishi J, Yamaguchi K (1989) Ferritin immunohistochemistry as a marker for microglia. *Acta Neuropathol* 79:129–136
  44. Jellinger KA, Paulus W, Grundke-Iqbal I, Riederer P, Youdim MB (1990) Brain iron and ferritin in Parkinson's and Alzheimer's diseases. *J Neural Transm Park Dis Dement Sect* 2:327–340
  45. Streit WJ, Braak H, Del Tredici K, Leyh J, Lier J, Khoshbouei H et al (2018) Microglial activation occurs late during preclinical Alzheimer's disease. *Glia* 66:2550–2562
  46. Nguyen AT, Wang K, Hu G, Wang X, Miao Z, Azevedo JA et al (2020) APOE and TREM2 regulate amyloid-responsive microglia in Alzheimer's disease. *Acta Neuropathol* 1:3
  47. Ayton S, Janelidze S, Roberts B, Palmqvist S, Kalinowski P, Diouf I et al (2020) Acute phase markers in CSF reveal inflammatory changes in Alzheimer's disease that intersect with pathology, APOE  $\epsilon$ 4, sex and age. *Prog Neurobiol* 47:101904
  48. Acosta-Cabrero J, Betts MJ, Cardenas-Blanco A, Yang S, Nestor PJ (2016) In vivo MRI mapping of brain iron deposition across the adult lifespan. *J Neurosci* 21:36
  49. Farrall AJ, Wardlaw JM (2009) Blood–brain barrier: ageing and microvascular disease—systematic review and meta-analysis. *Neurobiol Aging* 25:337–352
  50. Ward RJ, Zucca FA, Duyn JH, Crichton RR, Zecca L (2014) The role of iron in brain ageing and neurodegenerative disorders. *Lancet Neurol* 13:1045–1060
  51. Bulk M, Abdelmoula WM, Nabuurs RJA, van der Graaf LM, Mulders CWH, Mulder AA et al (2018) Postmortem MRI and histology demonstrate differential iron accumulation and cortical myelin organization in early- and late-onset Alzheimer's disease. *Neurobiol Aging* 62:231–242
  52. Nabuurs RJA, Hegeman I, Natté R, van Duinen SG, van Buchem MA, van der Weerd L et al (2011) High-field MRI of single histological slices using an inductively coupled, self-resonant microcoil: application to ex vivo samples of patients with Alzheimer's disease. *NMR Biomed* 24:251–357
  53. Dixon SJ, Stockwell BR (2014) The role of iron and reactive oxygen species in cell death. *Nat Chem Biol* 25:9–17
  54. Nakamura K, Kawakami T, Yamamoto N, Tomizawa M, Fujiwara T, Ishii T et al (2016) Activation of the NLRP3 inflammasome by cellular labile iron. *Exp Hematol* 44:116–124
  55. McIntosh A, Mela V, Harty C, Minogue AM, Costello DA, Kerskens C et al (2019) Iron accumulation in microglia triggers a cascade of events that leads to altered metabolism and compromised function in APP/PS1 mice. *Brain Pathol* 29:606–621
  56. Nnah IC, Lee C, Wessling-Resnick M (2020) Iron potentiates microglial interleukin-1 $\beta$  secretion induced by amyloid- $\beta$ . *J Neurochem* 154:177–189
  57. Ising C, Venegas C, Zhang S, Scheiblich H, Schmidt SV, Vieira-Saecker A et al (2019) NLRP3 inflammasome activation drives tau pathology. *Nature* 575:669–673
  58. Heneka MT, Kummer MP, Stutz A, Delekate A, Schwartz S, Vieira-Saecker A et al (2013) NLRP3 is activated in Alzheimer's disease and contributes to pathology in APP/PS1 mice. *Nature* 493:674–678
  59. Sankowski R, Böttcher C, Masuda T, Geirsdottir L, Sagar, Sindram E et al (2019) Mapping microglia states in the human brain through the integration of high-dimensional techniques. *Nat Neurosci* 22:2098–2110
  60. Böttcher C, Schlickeiser S, Sneeboer MAM, Kunkel D, Knop A, Paza E et al (2019) Human microglia regional heterogeneity and phenotypes determined by multiplexed single-cell mass cytometry. *Nat Neurosci* 22:78–90

### Publisher's Note

Springer Nature remains neutral with regard to jurisdictional claims in published maps and institutional affiliations.

Ready to submit your research? Choose BMC and benefit from:

- fast, convenient online submission
- thorough peer review by experienced researchers in your field
- rapid publication on acceptance
- support for research data, including large and complex data types
- gold Open Access which fosters wider collaboration and increased citations
- maximum visibility for your research: over 100M website views per year

At BMC, research is always in progress.

Learn more [biomedcentral.com/submissions](https://biomedcentral.com/submissions)

